



# Sonochemical Synthesis and Characterization of Ag/ZnO Heterostructure Nanocomposites and their Photocatalytic Efficiencies

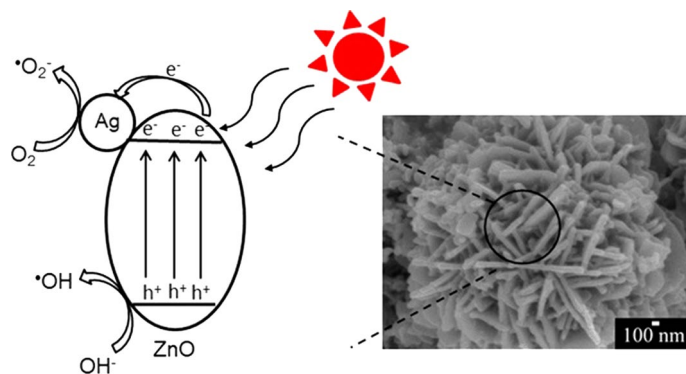
Saowaluk Buapoon<sup>1</sup> · Anukorn Phuruangrat<sup>1</sup> · Phattranit Dumrongrojthanath<sup>2</sup> · Titipun Thongtem<sup>3,4</sup> · Somchai Thongtem<sup>3,5</sup>

Received: 31 October 2020 / Accepted: 27 April 2021 / Published online: 21 May 2021  
© The Minerals, Metals & Materials Society 2021

## Abstract

Ag/ZnO heterostructure nanocomposites containing different amounts of Ag were successfully synthesized in surfactant-free solutions by a sonochemical deposition. The samples were characterized by x-ray diffraction (XRD), scanning electron microscopy (SEM), transmission electron microscopy (TEM), x-ray photoelectron spectroscopy (XPS), Fourier transform infrared (FTIR) spectroscopy and Raman spectroscopy. The results show that all heterostructure samples were composed of metallic Ag nanoparticles supported on top of nanoplate petals of hierarchical ZnO flowers. The photocatalytic properties of the samples were also evaluated through photodegradation of methylene blue (MB) and methyl orange (MO) as cationic and anionic model dyes under UV light irradiation. The photodegradation of MB and MO solutions containing Ag/ZnO heterostructure nanocomposites was higher than that of MB and MO solutions containing pure ZnO flowers because of the efficient separation and diffusion of photogenerated charge carriers through Ag/ZnO Schottky interface. Active species for MB and MO photodegradation were also investigated in this research.

## Graphical Abstract



**Keywords** Ag/ZnO hierarchical flowers · photocatalysis · radical scavengers · photostability · reusability

✉ Anukorn Phuruangrat  
phuruangrat@gmail.com

✉ Somchai Thongtem  
schthongtem@yahoo.com

<sup>1</sup> Division of Physical Science, Faculty of Science, Prince of Songkla University, Hat Yai, Songkhla 90112, Thailand

<sup>2</sup> Rajamangala University of Technology, Lanna Chiang Rai, Chiang Rai 57120, Thailand

<sup>3</sup> Materials Science Research Center, Faculty of Science, Chiang Mai University, Chiang Mai 50200, Thailand

<sup>4</sup> Department of Chemistry, Faculty of Science, Chiang Mai University, Chiang Mai 50200, Thailand

<sup>5</sup> Department of Physics and Materials Science, Faculty of Science, Chiang Mai University, Chiang Mai 50200, Thailand

## Introduction

At present, the fast growing population and industrialization have led to an increase of different environmental issues relating to living life on earth. Organic dyes from textile and leather production, including hazardous waste gases released from different industries are the major environmental contaminants.<sup>1–9</sup> Semiconductor photocatalysts are a promising material used to remove poisonous organic pollutants. Among different semiconductors, ZnO with wide band gap of  $\sim 3.37$  eV and large exciton binding energy of 60 meV is one of the most common materials that can be used for environmental treatment because of its outstanding optoelectronic properties, physical and chemical stability, low cost and non-toxic properties.<sup>1–3, 10–12</sup> In general, the properties and performance of ZnO are strongly controlled by its structure and morphology.<sup>13</sup> Three-dimensional (3D) hierarchical ZnO flowers have attracted remarkable attention for a number of applications relating to gas sensors and gas adsorption, and photodegradation and photovoltaic properties because ZnO flowers have large surface area and gas diffusion path higher than other morphologies.<sup>14, 15</sup> ZnO has excellent photocatalytic potential in degrading organic pollutants by transforming them into CO<sub>2</sub> and H<sub>2</sub>O better than TiO<sub>2</sub>.<sup>3, 16</sup> It is able to absorb a fraction of the UV spectrum with high energy better than TiO<sub>2</sub>.<sup>3</sup> Moreover, ZnO has some hindrance to fast recombination of photogenerated electron–hole pairs and low quantum yield of photocatalysis in aqueous solution.<sup>17</sup> Thus, improvement of photocatalytic performance of ZnO has become the most challenging for a number of researchers. To improve the photocatalytic performance of ZnO, noble metals such as Ag, Au, Pt and Pd as electronic trappers on the ZnO surface have been investigated in order to visualize interfacial charge diffusion, lower  $e^-/h^+$  recombination rate, improve electron trapping ability and induce surface plasmon resonance (SPR) process.<sup>18–23</sup> The optical, electrical, mechanical and antibacterial properties of heterostructure materials can be enhanced by incorporating with Ag. Thus, deposition of Ag nanoparticles has been intensively investigated.<sup>24</sup> There are many reports on the synthesis of heterostructure Ag/ZnO nanocomposites by hydrothermal/solvothermal method, radio frequency sputtering, sol-gel method and thermal decomposition.<sup>24–29</sup> Mostly, they are quite expensive and complex, have low growth rate products and are unable to control the aggregation of Ag nanoparticles loaded on top.<sup>15–20</sup> Compared to the sonochemical solution method as green chemistry, the aggregation of Ag nanoparticles can be prevented by the collapsed bubbles in a liquid irradiated by ultrasonic wave and the continuous growth of Ag nanoparticles.<sup>30–32</sup> Acoustic cavitation

is generated and an effective environment is supplied by transforming Ag<sup>+</sup> ions into Ag nanoparticles without the use of any severe reducing agent.<sup>32, 33</sup>

In this research, three-dimensional (3D) hierarchical ZnO flowers with high surface area and micro-pores loaded with different contents of Ag nanoparticles were synthesized by ultrasonic sonochemistry in a solution without any surfactant. The crystalline structure, morphology and chemical composition were characterized by x-ray diffraction (XRD), scanning electron microscopy (SEM), transmission electron microscopy (TEM), x-ray photoelectron spectroscopy (XPS), Fourier transform infrared (FTIR) spectroscopy and Raman spectroscopy. Photocatalytic properties of the samples were also evaluated through photodegradation of methylene blue (cationic dye) and methyl orange (anionic dye) under UV light irradiation.

## Experimental Procedure

Flower-like ZnO samples were prepared by direct precipitation. A 13.3866 g Zn(NO<sub>3</sub>)<sub>2</sub>·6H<sub>2</sub>O sample was dissolved in 200 ml reverse osmosis (R.O.) water under continued stirring. Subsequently, 40 ml of 3 M NaOH solution was added to the Zn<sup>2+</sup> solution under vigorous stirring for 24 h to form white precipitates. The precipitates were filtered, washed, dried and heated at 600°C at a 5°C min<sup>-1</sup> heating rate for 2 h in ambient atmosphere.

To prepare Ag/ZnO nanocomposites, different contents of AgNO<sub>3</sub> with 1%, 5% and 10% by weight of Ag were dissolved in 100 ml ethylene glycol containing 2.5 g ZnO suspension under constant stirring for 30 min. The mixtures were put in an ultrasonic bath and ultrasonically vibrated for 20 min. The as-prepared precipitates were collected, washed with deionized water and dried for further characterization.

Crystalline phases of the as-synthesized samples were analyzed by an x-ray diffractometer (XRD, Philips X'Pert MPD) using Cu-K<sub>α</sub> radiation in the 2θ range of 20°–70°. Morphological investigation was carried out by a field emission scanning electron microscope (FE-SEM, JEOL JSM-6335F) with an accelerating voltage of 20 kV coupled with an Oxford INCA energy dispersive x-ray spectrometer (EDS) and a transmission electron microscope (TEM, JEOL JEM 2010) with an acceleration voltage of 200 kV. A Fourier transform infrared spectrometer (Perkin Elmer FTIR Spectrometer Spectrum RX) was used in the range of 400–4000 cm<sup>-1</sup> at room temperature. The sample pellets for FTIR characterization were diluted by 40 times KBr. A Raman spectrometer (HORIBA Jobin Yvon T64000) was operated using 30 mW He-Ne laser with 632.8 nm wavelength. x-ray photoelectron spectroscopy (XPS) was carried out by a Kratos x-ray photoelectron spectrometer – Axis Ultra DLD with a monochromated Al K<sub>α</sub> radiation (1486.6

eV) as a providing source. All the XPS spectra were calibrated w.r.t. a C 1s electron peak at 285.1 eV.

Methylene blue (MB) and methyl orange (MO) as cationic and anionic model dyes were used as molecular probes for photocatalytic evaluation. The photocatalytic reaction was conducted under UV light at room temperature. The reaction was carried out using 200 mg catalyst dispersed in 200 ml of  $1 \times 10^{-5}$  M MB/MO aqueous solutions. Prior to irradiation, the suspension solution was magnetically stirred in the dark for 30 min to establish an adsorption/desorption equilibrium of methylene blue/methyl orange and photocatalyst. During photocatalytic testing, approximately 5 ml solution was sampled every 60 min and centrifuged to remove any suspended catalytic nanoparticles. The residual concentration of methylene blue/methyl orange contained in the cuvettes was measured at 665/465 nm with de-ionized water as a reference by a UV-visible spectrophotometer (Perkin-Elmer Lambda 25). The degradation efficiency was calculated by the below equation.

$$\text{Decolorization efficiency (\%)} = [(C_o - C_t)/C_o] \times 100 \quad (1)$$

$C_o$  is the initial dye concentration and  $C_t$  is the dye concentration after photocatalytic treatment for a period of time ( $t$ ).

## Results and Discussion

Figure 1 shows XRD patterns of ZnO prepared by direct precipitation at room temperature and Ag/ZnO composites prepared by sonochemical solution method. All the diffraction peaks of pure ZnO can be indexed to hexagonal ZnO with a

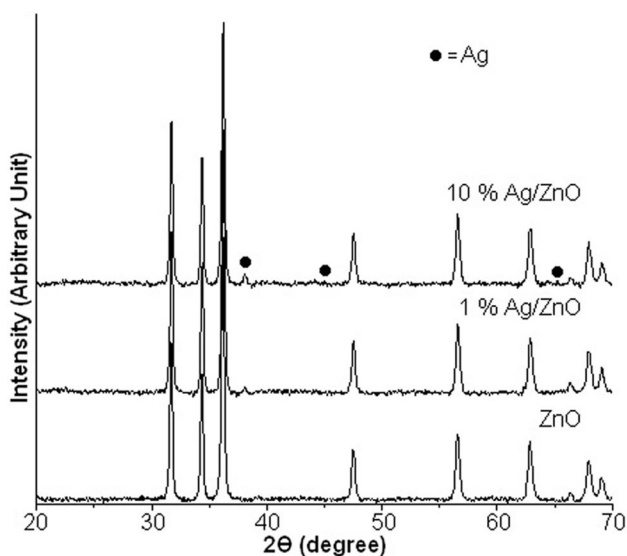


**Fig. 1** XRD patterns of pure ZnO, 1% Ag/ZnO and 10% Ag/ZnO flowers.

typical wurtzite structure (JCPDS No. 36-1451).<sup>34</sup> The XRD pattern of the pure ZnO sample shows the diffraction peaks at  $31.78^\circ$ ,  $34.45^\circ$ ,  $36.27^\circ$ ,  $47.59^\circ$  and  $56.64^\circ$  which can be indexed to the (100), (002), (101), (102) and (110) planes of the wurtzite-type hexagonal ZnO phase. The Ag/ZnO composites show three additional diffraction peaks at  $38.29^\circ$ ,  $44.49^\circ$  and  $64.52^\circ$  which can be indexed to the (111), (200) and (220) planes of the face-center-cubic (fcc) structure of silver (JCPDS No. 04-0783),<sup>34</sup> respectively. The diffraction peaks of Ag were strengthened by the increase of Ag content. No characteristic peaks of other phases, such as silver oxide were detected in the samples. These results verify that Ag/ZnO nanocomposites were successfully prepared by a one-step sonochemical method. The sharp diffraction peaks of both pure ZnO sample and heterostructure Ag/ZnO nanocomposites indicate that the samples are very good crystals. The diffraction peaks of ZnO containing in Ag/ZnO heterostructure nanocomposites remain unchanged as compared with those of pure ZnO sample. The results indicate that Ag ions did not incorporate in ZnO lattice as substituent or interstitial ions of host material. Thus, metallic fcc Ag nanoparticles were successfully deposited on top of ZnO nanoplates. Based on the Scherrer equation:  $D = 0.89\lambda/\beta\cos\theta$ , where  $\lambda$  is the wavelength of X-rays,  $\beta$  is the full width at half maximum (FWHM) of a diffraction peak,  $D$  is the particle size, and  $\theta$  is the diffraction angle.<sup>2,3</sup> The calculated average diameter of Ag nanoparticles was  $4.17 \pm 0.05$  nm.

The surface components and chemical states of pure ZnO and 10% Ag/ZnO nanocomposites were investigated by XPS as the results shown in Fig. 2. The full scan XPS survey spectra of the samples show only Zn and O for pure ZnO sample and additional Ag for 10% Ag/ZnO heterostructure nanocomposites. No other characteristic peaks were detected in the XPS survey spectra for the pure ZnO sample and 10% Ag/ZnO nanocomposites. The survey spectrum of 10% Ag/ZnO nanocomposites indicates that the product was composed of Ag nanoparticles deposited on top of ZnO nanoplates. The XPS spectrum of Ag 3d reveals two binding energy peaks at 367.2 eV and 373.2 eV corresponding to the Ag 3d<sub>5/2</sub> and Ag 3d<sub>3/2</sub> spin-orbit components of metallic silver.<sup>21,35,36</sup> Furthermore, the Ag 3d binding energy peaks of the as-prepared Ag/ZnO nanocomposites shifted to the lower energy side comparing with the Ag bulk (368.2 eV and 374.2 eV), respectively. The energy shift is primarily ascribed to the partial reduction of Ag<sup>+</sup> to Ag<sup>0</sup>, including the deposition of Ag on the ZnO sample with a small change of the Fermi level.<sup>35,36</sup> The XPS spectrum of Zn 2p shows two binding energy peaks at 1021.2 eV and 1044.4 eV for the ZnO sample and 1020.8 eV and 1044.0 eV for 10% Ag/ZnO nanocomposites which are attributed to Zn 2p<sub>3/2</sub> and Zn 2p<sub>1/2</sub>, respectively.<sup>1,17,21</sup> The Zn 2p peak has significantly split spin-orbit components of 23.2 eV which is close to that of the standard Zn<sup>2+</sup>. It can be seen that the Zn 2p binding

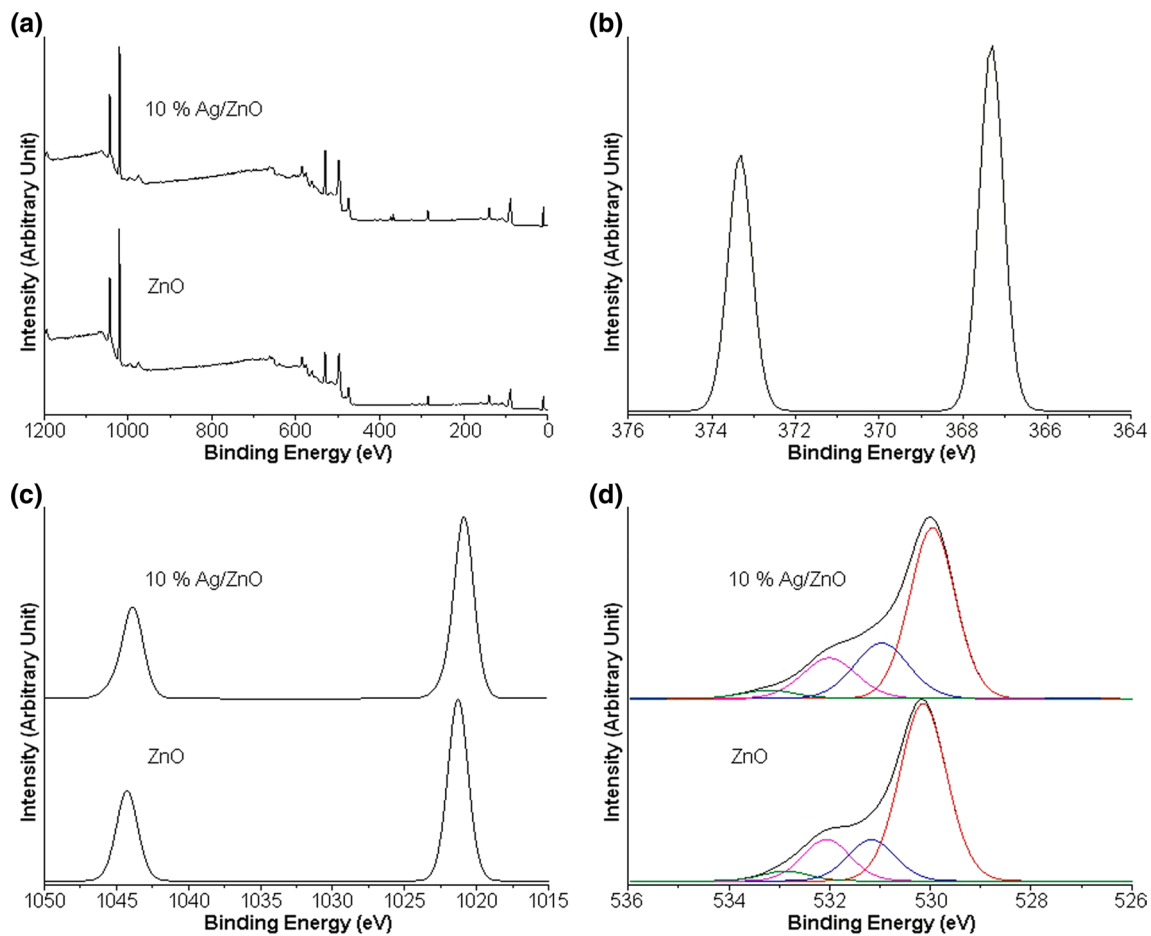


**Fig. 2** (a) Full XPS survey spectrum at 0–1200 eV and (b–d) high resolution XPS spectra of Ag 3d, Zn 2p and O 1s of ZnO and 10% Ag/ZnO flowers, respectively.

energies of Ag/ZnO heterostructure nanocomposites were shifted to the lower binding energy side with respect to pure ZnO sample because of the interaction of Ag nanoparticles and hierarchical flower-like ZnO structure. The asymmetric high-resolution XPS spectra of O 1s containing in pure ZnO sample and 10% Ag/ZnO nanocomposites can be de-convoluted into four Gaussian peaks at 530.16 eV, 531.1 eV, 532.0 eV and 532.8 eV for pure ZnO sample and 529.9 eV, 531.0 eV, 532.0 eV and 533.42 eV for 10% Ag/ZnO nanocomposites. They correspond with the Zn–O bond of ZnO crystal, surface oxygen vacancy and OH bonding of adsorbed H<sub>2</sub>O on top of the samples.<sup>1, 17, 21</sup>

SEM was used to investigate morphology of the as-prepared ZnO and Ag/ZnO samples as the results shown in Fig. 3. Clearly, the as-prepared sample was composed of ZnO flowers formed by nanoplate petals with smooth surfaces. The SEM images of 5% and 10% Ag/ZnO composites remained as flower-like structure in the same way as the pure ZnO sample. Ag spherical nanoparticles were detected

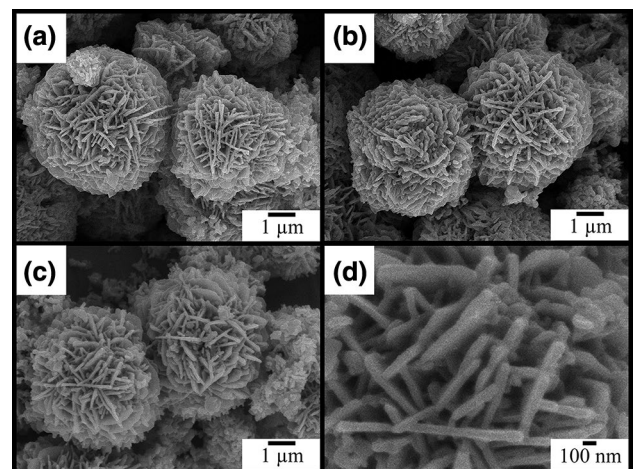


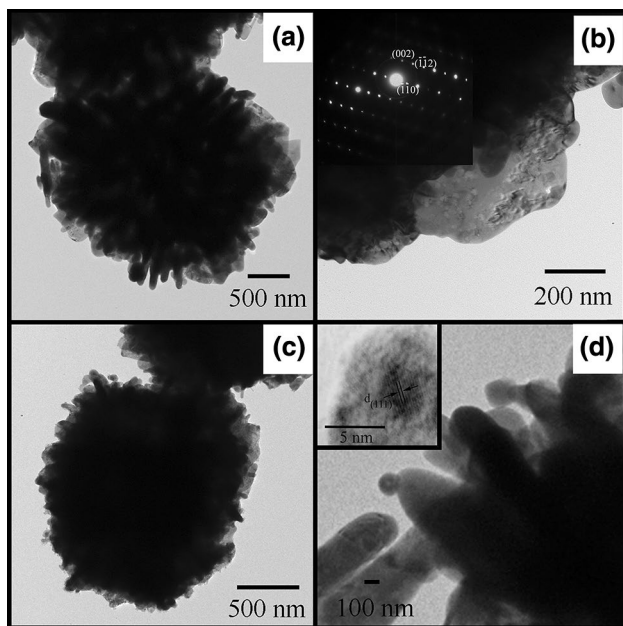
**Fig. 3** SEM images of (a) pure ZnO sample, (b) 5% Ag/ZnO nanocomposites and (c, d) 10% Ag/ZnO nanocomposites.

on the surface of ZnO flowers containing 5% and 10% Ag. They were suggested that ZnO flowers still maintained even after the deposition of Ag nanoparticles on top. The high-magnification FE-SEM image of 10% Ag/ZnO heterostructure nanocomposites clearly showed spherical Ag nanoparticles with particle size of 80–100 nm and good deposition on top of ZnO nanoplates. Furthermore, the coexistence of Ag and ZnO was analyzed by the energy dispersive x-ray spectroscopy (EDS) as the results shown in Fig. S1. Clearly, the heterostructure 10% Ag/ZnO nanocomposites contained only Ag, Zn and O without other elements. The EDS map of

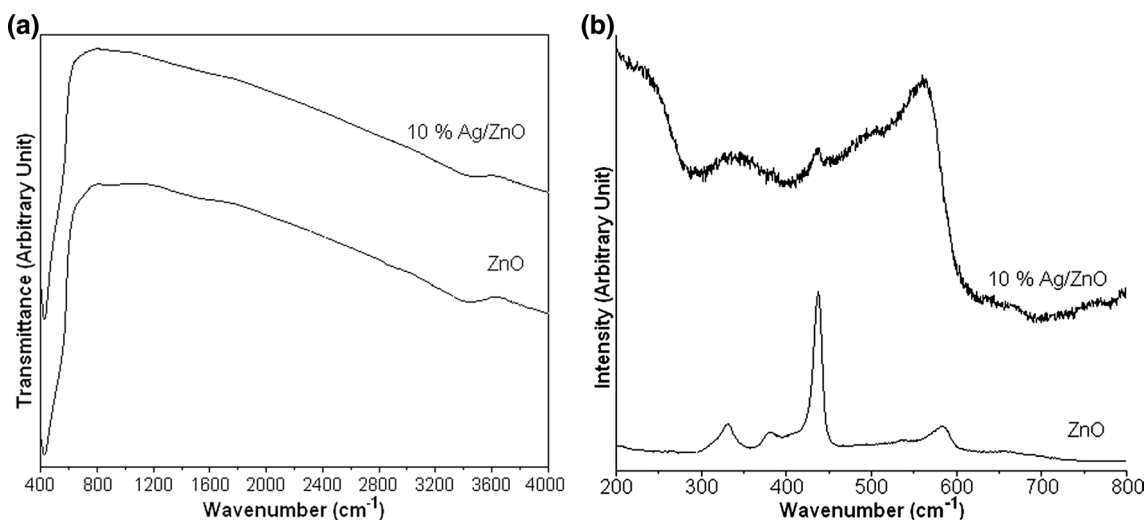
heterostructure 10% Ag/ZnO nanocomposites shows good distribution of Ag element on ZnO and the successful deposition of Ag nanoparticles on the surface of hierarchical ZnO flowers by the sonochemical method in accordance with the above XRD analysis.

Figure 4 shows typical low- and high-resolution TEM images and SAED pattern of ZnO flowers and flower-like 10% Ag/ZnO heterostructure nanocomposites. The TEM images of pure ZnO sample clearly demonstrate that the flowers were made up of thin nanoplate petals. A selected area electron diffraction (SAED) pattern of an individual ZnO nanoplate shows bright spots of electron diffraction which indicate the high crystalline wurtzite ZnO structure. The SAED pattern was indexed to the (002), (−1−12) and (−1−10) planes of wurtzite ZnO structure with zone axis of  $1-10$ . The TEM images of 10% Ag/ZnO heterostructure nanocomposites show spherical Ag nanoparticles with size of 60–80 nm deposited on the surface of flower-like ZnO structure. The high-magnification TEM image of 10% Ag/ZnO heterostructure nanocomposites shows strong interaction between Ag spherical nanoparticles and ZnO nanoplates. A high-resolution transmission electron microscopic (HRTEM) image of a single spherical Ag nanoparticle reveals a lattice space of the (111) crystallographic plane of the fcc Ag nanoparticle. Thus, the as-formed Schottky interface between the Ag noble metal and ZnO semiconductor played the role in enhancing the photocatalytic performance of ZnO flowers.

Figure 5a shows FTIR spectra of ZnO and Ag/ZnO samples. The transmittance band at  $425\text{ cm}^{-1}$  was assigned to the characteristic stretching mode of the Zn–O bond.<sup>1, 2, 16</sup> Bands at  $3424$  and  $1566\text{ cm}^{-1}$  were related to the stretching and bending modes of O–H groups,<sup>1, 2, 16</sup> respectively. The



**Fig. 4** TEM and HRTEM images, and SAED pattern of (a, b) ZnO and (c, d) 10% Ag/ZnO flowers.



**Fig. 5** (a) FTIR and (b) Raman spectra of pure ZnO sample and 10% Ag/ZnO nanocomposites.

FTIR analysis indicates the presence of surface adsorbed water molecules or hydroxyl groups on both the samples.

According to the group theory, the structure of ZnO with  $C_{6V}$  symmetry was predicted to contain one  $A_1$ , one  $E_1$ , two  $E_2$  and two  $B_1$  modes. The  $A_1$  mode and  $E_1$  mode are polar and split into transverse optical (TO) and longitudinal optical (LO) components which are both Raman and infrared (IR) active. The  $E_2$  mode is only Raman active, and the  $B_1$  mode is both IR and Raman inactive (silent).<sup>3, 37, 38</sup> Figure 5b shows the Raman spectra of ZnO and 10% Ag/ZnO samples within the wavenumber range of 200–800  $\text{cm}^{-1}$ . The Raman spectrum of the pure ZnO phase shows five peaks at 331  $\text{cm}^{-1}$ , 379  $\text{cm}^{-1}$ , 437  $\text{cm}^{-1}$ , 535  $\text{cm}^{-1}$  and 583  $\text{cm}^{-1}$ . The strong Raman peak at 437  $\text{cm}^{-1}$  was assigned to the characteristic  $E_2$ -mode of the wurtzite ZnO phase<sup>3, 38–40</sup> which clearly verifies the presence of high-quality typical wurtzite hexagonal ZnO flowers. The Raman peaks at 331 and 379  $\text{cm}^{-1}$  are related to  $E_{2H}$ – $E_{2L}$  and  $A_{1T}$  modes of ZnO which are associated with the vibration of heavy Zn sub-lattice and the vibration of oxygen atoms contained in wurtzite ZnO flowers.<sup>3, 38–40</sup> The broad Raman peak at 583  $\text{cm}^{-1}$  of pure ZnO is assigned to be the  $E_{1L}$  mode related to impurities and defects contained in the ZnO lattice.<sup>40</sup> The Raman spectrum of 10% Ag/ZnO nanocomposites shows the weak intensity  $E_2$  mode caused by a local strain of ZnO lattice close to the Ag–ZnO interface. A weak broad peak at 535  $\text{cm}^{-1}$  is a silent  $B_1$  mode and relates to the change in lattice strain and consequently results in lattice disorder.<sup>40</sup> It should be noted that the peak intensity of the 10% Ag/ZnO nanostructure is higher than that of the ZnO nanostructure because of the excitation of a localized surface plasmon of Ag nanoparticles deposited on ZnO nanoplates, caused by the formation of charge transfer complexes and bond forming between Ag species and ZnO surface, localized formed electric field interaction with optical phonon and enhanced scattering intensity of active phonon.<sup>41</sup> In addition, the structure of 10% Ag/ZnO nanocomposites is more open than that of pure ZnO. Thus, the vibration amplitude and peak intensity of the 10% Ag/ZnO nanostructure are higher than those of the pure ZnO sample.

Photocatalytic activities of the Ag/ZnO heterostructure nanocomposites with different weight contents of the loaded Ag nanoparticles were investigated through the degradation of MB and MO under UV light irradiation within 300 min. Figure S2 shows the absorbance versus wavelength for the degradation of MB and MO over the pure ZnO sample and 10% Ag/ZnO heterostructure nanocomposites within different lengths of irradiation time. The intensities of UV-visible absorption of MB and MO were decreased with an increase in the reaction time under UV light irradiation. Clearly, the characteristic peaks of MB dye at 665 nm and MO dye at 465 nm over 10% Ag/ZnO heterostructure nanocomposites

are lower than those of MB and MO over the pure ZnO sample. The results indicate that 10% Ag/ZnO heterostructure nanocomposites have the highest photocatalytic activity in degrading of MB and MO under UV light irradiation.

The photocatalytic degradation of MB and MO by different photocatalysts (Fig. 6a and b) was tested under UV visible light irradiation within 300 min. The MB and MO solutions without the photocatalyst as the blank test show insignificant self-photolysis under UV light irradiation. In this research, the MB and MO degradation rates in the solutions containing pure ZnO were about 37% and 23% which were ascribed to the high recombination rate of photogenerated electron–hole pairs. The photocatalytic efficiencies of 1% Ag/ZnO, 5% Ag/ZnO and 10% Ag/ZnO nanocomposites were about 60%, 73% and 97% for photodegradation of MB and 41%, 56% and 63% for photodegradation of MO, respectively. The photocatalytic activities of the photocatalysts for both MB and MO degradation are in sequence as follows: pure ZnO < 1% Ag/ZnO < 5% Ag/ZnO < 10% Ag/ZnO. Interestingly, the photocatalytic activities for MB and MO solutions over 10% Ag/ZnO nanocomposites are, respectively, 2.62 and 2.74 times of those for MB and MO solutions over the ZnO sample because of the effective separation and diffusion of the photogenerated charge carriers.<sup>19, 22</sup>

To have a better understand for the degradation kinetics of MB and MO dyes, the experimental data were fitted to the pseudo-first-order simplification of Langmuir–Hinshelwood kinetics through a well-established photocatalysis of a low initial pollutant concentration as follows.

$$\ln C_o/C_t = k_{app}t \quad (2)$$

$C_o$  and  $C_t$  are the dye concentration at the initial and time  $t$ , respectively. The  $k_{app}$  is the apparent first-order rate constant ( $\text{min}^{-1}$ )<sup>2, 3, 16, 18</sup> obtained from the gradient of the  $\ln(C_o/C_t)$  versus time plot, and the results are shown Fig. 6c and d. All the plots were fitted to linear lines. Thus, the photocatalytic reaction follows the pseudo-first-order kinetics. It can be seen that weight content of the loaded Ag nanoparticles has strong influence on the photocatalytic activity of the Ag/ZnO photocatalyst. The 10% Ag/ZnO nanocomposites have the highest apparent rate constants of  $0.0111 \text{ min}^{-1}$  for MB degradation and  $3.68 \times 10^{-3} \text{ min}^{-1}$  for MO degradation which are about 6.98 and 4.31 times of those of pure ZnO for the degradation of both dyes ( $1.59 \times 10^{-3} \text{ min}^{-1}$  for MB and  $8.53 \times 10^{-4} \text{ min}^{-1}$  for MO), respectively.

During UV irradiation, electrons in valence band of ZnO were excited to conduction band, leading to the creation of photoinduced holes in valence band. These photoexcited electrons further diffused to Ag nanoparticles and were captured by the adsorbed  $O_2$  to form superoxide anion radical ( $O_2^-$ ). Concurrently, the photoinduced holes were captured by  $OH^-$  and  $H_2O$  to form hydroxyl radical (OH, the neutral

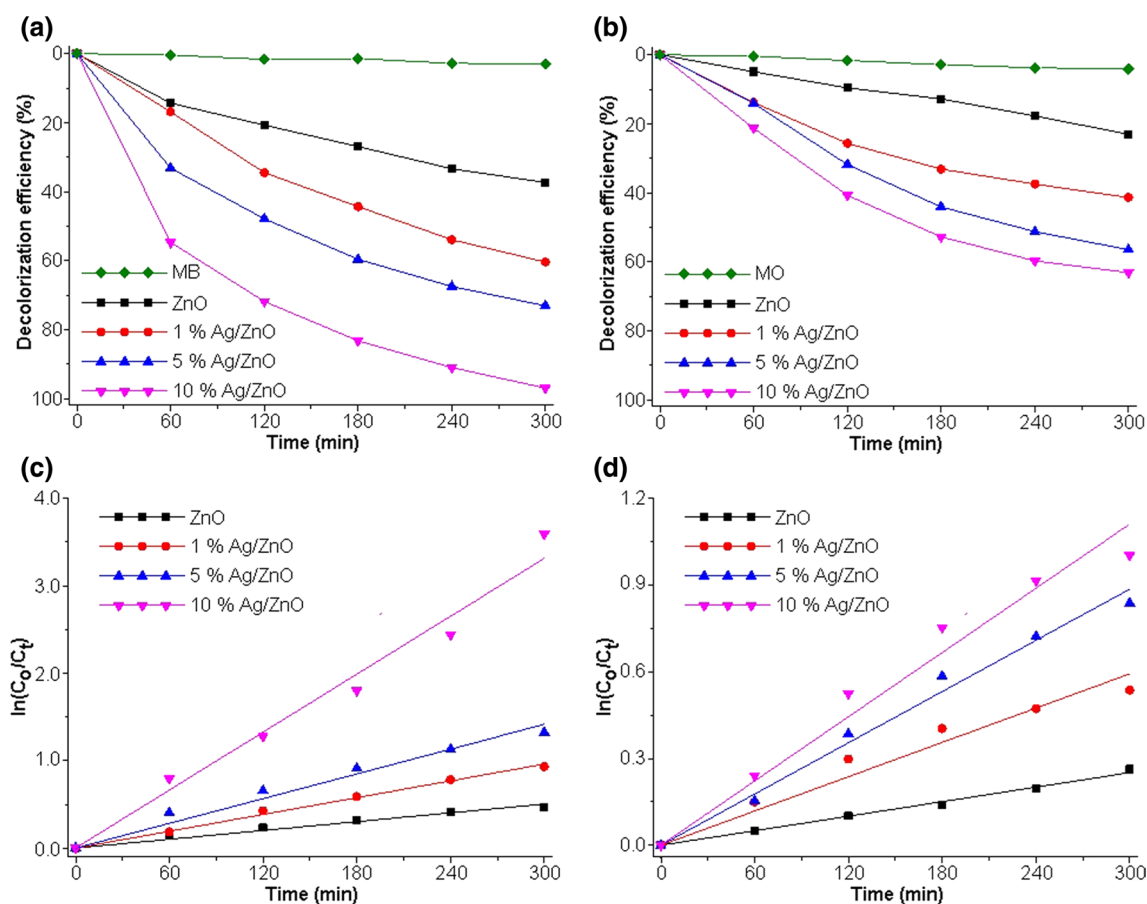


**Fig. 6** Decolorization efficiencies and pseudo-first-order plots for photodegradation of (a, c) MB and (b, d) MO over ZnO flowers containing 0%, 1%, 5% and 10% Ag nanoparticles under UV light irradiation comparing with decolorization efficiencies of the blank test of MB and MO.

form of hydroxide ion ( $\text{OH}^-$ )).<sup>2, 3, 16</sup> These active species degraded the MB and MO molecules by transforming the dyes into  $\text{CO}_2$  and  $\text{H}_2\text{O}$  as final products.<sup>2, 3, 16</sup> The Ag/ZnO nanocomposites have photocatalytic activity higher than pure ZnO because Ag nanoparticles on ZnO petals acted as electron sinks by providing accumulation sites of electrons and improved electron–hole separation.<sup>19, 20, 22</sup> Thus, the most effective electron–hole separation of Ag/ZnO nanocomposites is attributed to achieve the highest photocatalytic efficiency.<sup>19, 20, 22</sup>

To further investigate active species relating with the photodegradation of MB and MO dyes over Ag/ZnO nanocomposites, triethanolamine (TEOA), isopropyl alcohol (IPA) and benzoquinone (BQ) were used to scavenge holes ( $\text{h}^+$ ), hydroxyl radicals ( $\text{OH}$ ) and superoxide anions ( $\text{O}_2^-$ ) during the photocatalytic process<sup>42–45</sup> as the results shown in Fig. 7a and b. The photodegradation of MB and MO solutions containing Ag/ZnO nanocomposites significantly decreased with the addition of both IPA and BQ under UV

light irradiation. The photodegradation rates of MB and MO in the presence of Ag/ZnO nanocomposites were 15% and 11% for IPA adding, 36% and 22% for BQ adding, and 79% and 48% for TEOA adding, respectively. Thus,  $\text{OH}$  and  $\text{O}_2^-$  played the important role in the degradation of MB and MO solutions containing Ag/ZnO nanocomposites under UV light irradiation.

Figure 7c and d shows the reusability of Ag/ZnO nanocomposites for MB and MO degradation within five cycles under UV light irradiation. The photocatalyst was separated, thoroughly washed and dried for the next cycle. In this research, the photodegradation rates of MB and MO solutions containing the reused 10% Ag/ZnO nanocomposites were decreased to 95% and 56% after five cycles. The photocatalytic efficiencies at the end of cycle five of 10% Ag/ZnO nanocomposites for both MB and MO degradation were little lessened as compared with those at the end of cycle one. Thus, the 10% Ag/ZnO nanocomposites are quite stable for photodegradation of MB and MO dyes under UV light irradiation.

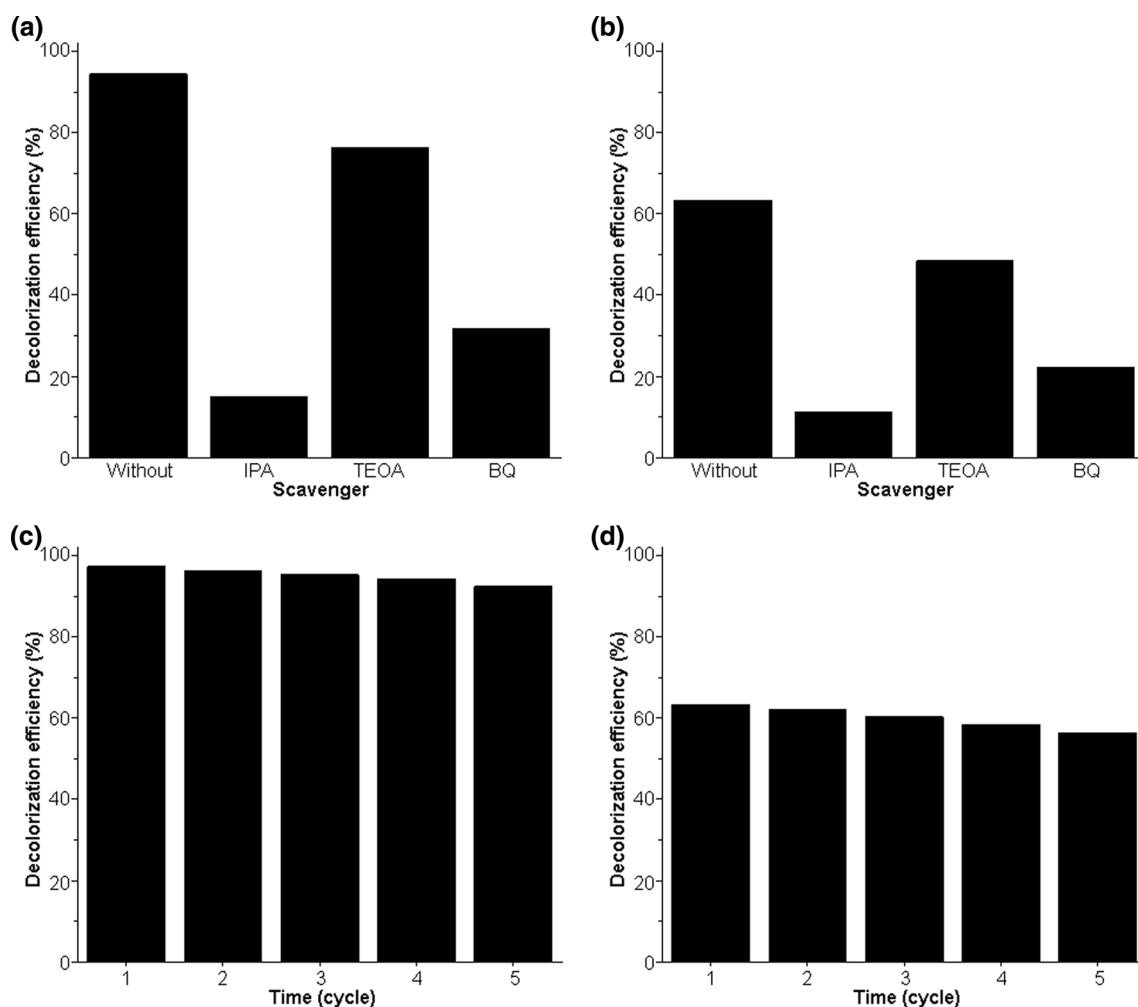


**Fig. 7** (a, b) Effect of different scavengers on photodegradation of MB and MO over 10% Ag/ZnO nanocomposites, and (c, d) photostability and reusability of 10% Ag/ZnO nanocomposites used for photodegradation of MB and MO under UV light irradiation within five cycles.

## Conclusions

The heterostructure Ag/ZnO nanocomposites containing different Ag contents were successfully prepared by a simple sonochemical solution method without the use of a surfactant. The Ag/ZnO heterostructure nanocomposites have excellent photocatalytic activities that are higher than the pure ZnO sample. The results were attributed to promote the effective generation, separation and diffusion of photoinduced charges at Ag/ZnO interfaces, including a consequent reduction of electron–hole recombination rate. The nanocomposites are promising materials used for photocatalysis, photovoltaic devices and solar-energy conversion.

**Supplementary Information** The online version contains supplementary material available at <https://doi.org/10.1007/s11664-021-08985-7>.

**Acknowledgments** The research was supported through the Contract No. 1-2562-02-014, Faculty of Science Research Fund, Faculty of Science, Prince of Songkla University, Hat Yai, Songkhla 90112, Thailand, and the Program Management Unit for Human Resources & Institutional Development, Research and Innovation, Office of National Higher Education Science Research and Innovation Policy Council (NXPO) [Grant Number B16F640001].

**Conflict of interest** The authors declare that they have no conflict of interest.

## References

1. V.H. Thi, and B.K. Lee, *Mater. Res. Bull.* 96, 171 (2017).
2. S. Bhatia, N. Verma, and R. Kumar, *J. Alloy. Compd.* 726, 1274 (2017).



3. O. Yayapao, T. Thongtem, A. Phuruangrat, and S. Thongtem, *Mater. Sci. Semicond. Process.* 39, 786 (2015).
4. G. Chen, Y. Li, M. Bick, and J. Chen, *Chem. Rev.* 120, 3668 (2020).
5. J. Chen, Y. Huang, N. Zhang, H. Zou, R. Liu, C. Tao, X. Fan, and Z.L. Wang, *Nat. Energy* 1, 16138 (2016).
6. K. Meng, S. Zhao, Y. Zhou, Y. Wu, S. Zhang, Q. He, X. Wang, Z. Zhou, W. Fan, X. Tan, J. Yang, and J. Chen, *Matter* 2, 896 (2020).
7. L. Jin, X. Xiao, W. Deng, A. Nashalian, D. He, V. Raveendran, C. Yan, H. Su, X. Chu, T. Yang, W. Li, W. Yang, and J. Chen, *Nano Lett.* 20, 6404 (2020).
8. C. Yan, Y. Gao, S. Zhao, S. Zhang, Y. Zhou, W. Deng, Z. Li, G. Jiang, L. Jin, G. Tian, T. Yang, X. Chu, D. Xiong, Z. Wang, Y. Li, W. Yang and J. Chen, *Nano Energy* 67, 104235 (2020).
9. J. Xu, Y. Zou, A. Nashalian and J. Chen, *Front. Chem.* 8, 577327 (2020).
10. R. Yu, C. Pan, J. Chen, G. Zhu, and Z.L. Wang, *Adv. Funct. Mater.* 23, 5868 (2013).
11. Q. Yang, Y. Liu, C. Pan, J. Chen X. Wen, and Z.L. Wang, *Nano Lett.* 13, 607 (2013).
12. C. Yan, W. Deng, L. Jin, T. Yang, Z. Wang, X. Chu, H. Su, J. Chen, W. Yang, and A.C.S. Appl, *Mater. Interfaces* 10, 41070 (2018).
13. Y. Li, H.F. Zuo, Y.R. Guo, T.T. Miao, and Q.J. Pan, *Res. Lett.* 11, 260 (2016).
14. F. Liao, X. Han, Y. Zhang, C. Xu, and H. Chen, *J. Mater. Sci.* 28, 16855 (2017).
15. K. Ahmada, and S.M. Mobin, *Nanoscale Adv.* 1, 719 (2019).
16. M. Ahmad, E. Ahmed, Y. Zhang, N.R. Khalid, J. Xu, M. Ullah, and Z. Hong, *Curr. Appl. Phys.* 13, 697 (2013).
17. H.J. Lee, J.H. Kim, S.S. Park, S.S. Hong, and G.D. Lee, *J. Indus. Eng. Chem.* 25, 199 (2015).
18. C.H. Le, O.T.T. Nguyen, H.S. Nguyen, L.D. Pham, and C.V. Hoang, *Curr. Appl. Phys.* 17, 1506 (2017).
19. Y. Liu, C. Xu, Z. Zhu, J. Lu, A.G. Manohari, and Z. Shi, *Mater. Res. Bull.* 98, 64 (2018).
20. M. Stucchi, C.L. Bianchi, C. Argirisus, V. Pifferi, B. Neppolian, G. Cerrato, and D.C. Boffito, *Ultrason. Sonochem.* 40, 282 (2018).
21. V. Vaiano M. Matarangolo, J.J. Murcia, H. Rojas, J.A. Navío and M.C. Hidalgo, *Appl. Catal. B* 225, 197 (2018).
22. L. Muñoz-Fernandez, A. Sierra-Fernandez, O. Milošević, and M.E. Rabanal, *Adv. Powder Tech.* 27, 983 (2016).
23. Y.F. Cheng, W. Jiao, Q. Li, Y. Zhang, S. Li, D. Li, and R. Che, *J. Colloid Interf. Sci.* 509, 58 (2018).
24. J.T. Park, C.S. Lee, C.H. Park, and J.H. Kim, *Chem. Phys. Lett.* 685, 119 (2017).
25. B. Sarma, and B.K. Sarma, *Appl. Surf. Sci.* 410, 557 (2017).
26. Y. Wei, X. Wang, G. Yi, L. Zhou, J. Cao, G. Sun, Z. Chen, H. Bala, and Z. Zhang, *Mater. Sci. Semicond. Process.* 75, 327 (2018).
27. V.V.S. Kumar, and D. Kanjilal, *Mater. Sci. Semicond. Process.* 81, 22 (2018).
28. Y. Zheng, L. Zheng, Y. Zhan, X. Lin, Q. Zheng, and K. Wei, *Inorg. Chem.* 46, 6980 (2007).
29. B. Subash, B. Krishnakumar, M. Swaminathan, and M. Shanthi, *Langmuir* 29, 939 (2013).
30. H. Xu, and K.S. Suslick, *ACS Nano* 4, 3209 (2010).
31. P.P. Goswami, H.A. Choudhury, S. Chakma, and V.S. Moholkar, *Ind. Eng. Chem. Res.* 52, 17848 (2013).
32. S. Ganguly, P. Das, M. Bose, T.K. Das, S. Mondal, A.K. Das, and N.C. Das, *Ultrason. Sonochem.* 39, 577 (2017).
33. M. Faried, K. Shameli, M. Miyake, H. Hara and N.B.A. khairudin (2015) *Dig. J. Nanomater. Biostructures* 10, 1419
34. Powder Diffract. File, JCPDS Internat. Centre Diffract. Data, PA 19073–3273, U.S.A. (2001).
35. F. Sun, X. Qiao, F. Tan, W. Wang, and X. Qiu, *J. Mater. Sci.* 47, 7262 (2012).
36. Y.H. Lu, M. Xu, L.X. Xu, C.L. Zhang, Q.P. Zhang, X.N. Xu, S. Xu, and K. Ostrikov, *J. Nanopart. Res.* 17, 350 (2015).
37. U. Routray, R. Dash, J.R. Mohapatra, J. Das, V.V. Srinivasu, and D.K. Mishra, *Mater. Lett.* 137, 29 (2014).
38. A. Phuruangrat, S. Thongtem, and T. Thongtem, *Mater. Design* 107, 250 (2016).
39. M.A. Alvi, A.A. Al-Ghamdi, and M.S. Akhtar, *Mater. Lett.* 204, 12 (2017).
40. N. Gogurla, S. Bayan, P. Chakrabarty, and S.K. Ray, *J. Lumin.* 194, 15 (2018).
41. Reza Zamiri, Avito Rebelo, Golriz Zamiri, Atena Adnani, Ajay Kuashal, Michael Scott Belsley and J. M. F. Ferreira, *RSC Adv.* 4, 40902 (2014).
42. A. Habibi-Yangjeh, and M. Shekofteh-Gohari, *Prog. Nat. Sci.-Mater.* 29, 145 (2019).
43. M. Massaro, M. Casiello, L. D'Accolti, G. Lazzara, A. Nacci, G. Nicotra, R. Noto, A. Pettignano, C. Spinella and S. Riela, *Appl. Clay Sci.* 189, 105527 (2020).
44. B. Babu, R. Koutavarapu, J. Shim and K. Yoo, *Mater. Sci. Semicond. Process.* 107, 104834 (2020).
45. C. Feng, Z. Chen, J. Jing, and J. Hou, *J. Mater. Chem. C* 8, 3000 (2020).

**Publisher's Note** Springer Nature remains neutral with regard to jurisdictional claims in published maps and institutional affiliations.